

Quantum Classical Algorithm for the Study of Phase Transitions in the Hubbard Model via Dynamical Mean-Field Theory

Anshumitra Baul

Department of Physics and Astronomy, Louisiana State University, Baton Rouge, Louisiana 70803, USA

Herbert F Fotso

Department of Physics, University at Buffalo, Buffalo, NY 14260, USA

Hanna Terletska

Department of Physics and Astronomy, Middle Tennessee State University, Murfreesboro, TN 37132, USA

Juana Moreno and Ka-Ming Tam

*Department of Physics and Astronomy, Louisiana State University, Baton Rouge, Louisiana 70803, USA and
Center for Computation and Technology, Louisiana State University, Baton Rouge, LA 70803, USA*

(Dated: August 4, 2023)

Simulating quantum many-body systems is believed to be one of the most promising applications of near-term noisy quantum computers. However, in the near term, system size limitation will remain a severe barrier for applications in materials science or strongly correlated systems. A promising avenue of research is to combine many-body physics with machine learning for the classification of distinct phases. In this paper, we propose a workflow that synergizes quantum computing, many-body theory, and quantum machine learning (QML) for studying strongly correlated systems. In particular, it can capture a putative quantum phase transition of the stereotypical strongly correlated system, the Hubbard model. Following the recent proposal of the hybrid classical-quantum algorithm for the two-site dynamical mean-field theory (DMFT), we present a modification that allows the self-consistent solution of the single bath site DMFT. The modified algorithm can easily be generalized for multiple bath sites. This approach is used to generate a database of zero-temperature wavefunctions of the Hubbard model within the DMFT approximation. We then use a QML algorithm to distinguish between the metallic phase and the Mott insulator phase to capture the metal-to-Mott insulator phase transition. We train a quantum convolutional neural network (QCNN) and then utilize the QCNN as a quantum classifier to capture the phase transition region. This work provides a recipe for application to other phase transitions in strongly correlated systems and represents an exciting application of small-scale quantum devices realizable with near-term technology.

I. INTRODUCTION

Strong electronic interactions in quantum materials give rise to many physical phenomena of technological interest. Some notable effects include the Mott metal-insulator transition, heavy fermions, fractional quantum effects, frustrated magnetism, and non-Fermi liquid metals [1–3]. It is notoriously difficult to study strongly correlated systems, as there is usually no good starting point for perturbative methods. For example, the superconducting cuprates have been studied intensively for over three decades, and there is still no consensus on the mechanism for their superconducting property [4, 5]. A plethora of classical numerical methods has been employed to solve simplified models of strongly correlated systems such as the Hubbard model [6, 7]. However, these methods are often constrained by the minus sign problem for Quantum Monte Carlo (QMC), or by the exponential scaling of the Hilbert space with the system sizes for exact diagonalization. This prevents simulations from attaining low temperatures where sought-after properties are believed to occur.

Embedding schemes are viable alternatives for the treatment of many-body problems in the thermodynamic

limit. The dynamical mean field theory (DMFT) [8–13], which maps the lattice problem onto a simple impurity problem, is a frequently used embedding scheme. This method solves some of the important problems in strongly correlated systems in the high dimensional limit. Particularly, it captures the metal-insulator transition without biased approximation [9].

The DMFT mapping is exact in the limit of infinite spatial dimensions but is approximate for finite dimensions. The approximation can be improved by systematically incorporating corrections due to the spatial dependence of the model. There are two major methods to include spatial correlations: perturbative approaches [14–19], and impurity cluster approaches using more than one impurity [20–22]. The latter, in principle, provides an exact calculation up to the finite cluster size. Thanks to the new formulation of various numerical algorithms and advances in computing power, the single impurity problem can be solved numerically with high accuracy. Over the past few years, a new approach based on techniques from data science and machine learning has also been proposed for the single impurity problem [23–27]. In contrast with the single impurity case, when dealing with problems involving multiple impurity sites, more ad-

vanced versions of DMFT like dynamical cluster approximation (DCA) [20, 21] and Cellular DMFT (CDMFT) [22] are needed. These methods, which partially restore spatial fluctuations, require solving systems that explicitly involve multiple impurity sites. Solving such problems remains a major bottleneck for numerical studies.

Classical computing approaches for numerically accurate solutions of strongly correlated systems suffer from the exponential scaling of either computing time (minus sign problem in QMC) or of the storage (e.g for exact diagonalization and other Hamiltonian based real space renormalization methods). This poor scaling leads to the inability to make predictions for large systems. This has always been an important issue for numerical methods on strongly correlated systems and it is unlikely to be resolved by a breakthrough on classical hardware or algorithm.

The advancement of quantum computing hardware and algorithm provides a new avenue for the study of strongly correlated systems. It has been shown that the DMFT approach can be implemented as a hybrid quantum-classical scheme [28–30]. In this context, quantum hardware is used to solve the effective impurity problem from the DMFT algorithm. The result is then post-processed by a classical computer to extract the value of hybridization parameters.

While the direct simulation of a model with explicit electron-electron interaction, such as the Hubbard model, near the thermodynamic limit would require presently out-of-reach qubit resources. However, performing DMFT simulations on a noisy intermediate-scale quantum (NISQ) device is feasible because the impurity problem can be approximated using only a few lattice sites. A major hurdle for the DMFT solution in the quantum-classical hybrid scheme is the requirement to compute excited states or Green’s functions, which presents a challenge for quantum computers [31].

There is a unique problem when using a quantum computing approach to solve the DMFT. The number of sites/qubits available is still rather limited. The DMFT requires the calculation of the excited state. In fact, formally, the DMFT requires the full excitation spectrum. In the infinite dimension limit, the excitation spectrum is obviously a continuous function of energy in a metallic phase. Unfortunately, with the very limited number of sites, that is the limited Hilbert space dimension, the continuous spectrum is represented by a set of discrete delta functions. In order to make the calculations possible, some kind of arbitrary smoothing process needs to be employed to transform the set of delta functions into a continuous function. The problem is particularly severe for extracting physical quantities. For a generic fermionic system, the equilibrium physical properties are largely determined by the degrees of freedom around the Fermi level. In this context, it is valuable to devise a procedure to interpret the results, e.g. drawing the phase boundaries, without directly calculating quantities on the Fermi level.

Given the above motivation, we propose to intersect many-body physics, via DMFT, and machine learning (ML) for the classification of different phases. This amalgamation has become an emergent area of research with great success [32–34]. Many different formulations of ML methods have been applied to the study of phase transitions of both classical and quantum-interacting systems. A natural data input for ML applied to a quantum system is the quantum wavefunction. Unfortunately, classical ML is not originally formulated for quantum systems. Therefore one has to preprocess the data either by collapsing the wavefunction onto some other quantities such as density matrix or entanglement entropy [35], or formulate the quantum systems in terms of path integral and treat it as an effective classical system [36–38].

There is an extensive number of studies on using the classical ML approach to locate phase transition both for classical and quantum systems [36–50]. Quantum machine learning (QML) is a new paradigm that allows input to be represented in terms of wavefunctions. Over the past couple of years, QML has been applied to studies of phase transitions in many-body systems [51–53]. Similar to the idea in classical ML applications, the quantum states are thought to match data instances of particular parameters with a label to the corresponding phase. The task here is to discriminate data instances with different labels, similar to classical ML approaches.

The exploration of quantum circuits as a classifier began a decade ago [54–57]. The concept of quantum classifiers has been infused with the principles of classical neural networks in the past few years [36, 58–72]. Convolutional neural network (CNN) [73] is designed to acquire a broad range of features from the correlation functions of complex systems with many interacting components, allowing for the identification of different phases of matter and their corresponding phase transitions. This technique involves compressing and reducing the degrees of freedom, which has led to the proposal that the concept of the renormalization group may be applicable in some neural networks [74–80].

The application of CNNs in physics has been extensive, ranging from learning patterns from statistical models to strongly correlated systems [33, 81]. The incorporation of convolutional layers in each layer of activation functions in a dense neural network allows for the extraction of hidden information by combining local data, a feature lacking in the standard dense neural network [82]. In quantum circuits, this can be achieved by replacing links and activation functions with quantum links and gates, respectively, resulting in a quantum neural network classifier with convolutional layers that can process convolution between nearby qubits [83].

QCNN is a quantum circuit model which extends the key properties of the classical CNN to the quantum domain. The circuit’s input is a quantum state. The Quantum Convolutional Layer consists of a series of two-qubit unitary operators, which establishes correlations between the qubits in the circuit. In the Quantum Pooling Layer,

the number of qubits is reduced by performing operations upon each until a specific point and then we disregard some of the qubits in a specific layer. We define a 'pooling layer' where we stop performing operations on certain qubits. The convolution and pooling layers are added to the circuit until the system size (the remaining number of qubits) is sufficiently small, after which a fully connected layer is applied as a unitary function on the remaining qubits. The outcome is determined by measuring a fixed number of output qubits, with hyperparameters such as the number of convolution and pooling layers fixed.

Recent studies have shown that quantum-enhanced ML is a promising approach for recognizing phases of matter [84]. Using the QCNN method, it may be possible to identify different phases of a quantum many-body system, representing a significant step toward detecting quantum phase transitions. The advantage of using the QCNN approach is that the input is naturally quantum mechanical, eliminating the need to represent the wavefunction as a classical vector whose dimension grows exponentially with respect to the system size [85]. The required input should consist of a quantum circuit and the most effective approach for obtaining the wavefunction through the DMFT solution of the two-site single impurity Anderson Model (SIAM) is the variational quantum eigensolver (VQE) method executed on NISQ computers. The present study aims to use the QCNN to identify the VQE wavefunction corresponding to different phases of the model and provide a possible framework for extracting quantum critical points in a many-body quantum system solved by VQE.

This paper presents a viable recipe for the study of strongly correlated systems. Specifically, we focus on drawing the phase diagram. The idea combines DMFT, VQE, and QML. The entire process can be implemented on NISQ computers except that the optimization of the parameters is done by classical algorithms. The paper is organized as follows. In Section II, we briefly describe the DMFT approach and its relation to the SIAM. In Section III, the methods and procedure of the two-site DMFT are presented. The quantum simulation of the two-site Hubbard model is described in Section IV. The results for the impurity Green's function, quasi-particle weight, and entanglement entropy are presented in section V

In section VI, we use the wave function from the DMFT solution to train a QCNN for the detection of the metal-to-insulator phase transition. The results after training the QCNN for the classification of different phases are shown in section VII. We conclude and propose possible future directions of using VQE and QML methods via DMFT for the study of strongly correlated systems.

II. DYNAMICAL MEAN FIELD THEORY

Our starting point for strongly correlated electrons is the Hubbard model defined by the Hamiltonian:

$$H = - \sum_{\langle i,j \rangle \sigma} t_{ij} (\hat{c}_{i,\sigma}^\dagger \hat{c}_{j,\sigma} + h.c) + U \sum_j \hat{n}_{j,\downarrow} \hat{n}_{j,\uparrow} \quad (1)$$

where the electrons hop between adjacent lattice sites i and j , denoted by $\langle i,j \rangle$, with amplitude $t_{ij} = t$. $\hat{c}_{i,\sigma}^\dagger$ and $\hat{c}_{i,\sigma}$ respectively denote the creation and annihilation operators for an electron of spin σ at site i . $\hat{n}_{j,\sigma}$ is the number of particles with spin σ at the site j . The interaction between electrons is governed by the on-site Coulomb repulsion, of strength U .

DMFT is a generalization of the usual mean-field theory for classical systems to the quantum fermionic systems on a lattice. As in conventional mean-field theory, it neglects spatial fluctuations however it explicitly addresses temporal fluctuations.

The action of the Hubbard model on a lattice in d dimension can be written as

$$S = - \sum_{\mathbf{r}_i, \mathbf{r}_j, \sigma} \int_0^\beta \int_0^\beta d\tau_i d\tau_j \psi_\sigma^\dagger(\mathbf{r}_i, \tau_i) G_0^{-1}(\mathbf{r}_i, \tau_i, \mathbf{r}_j, \tau_j) \psi_\sigma(\mathbf{r}_j, \tau_j) + U \sum_{\mathbf{r}_i} \int_0^\beta d\tau_i \psi_\uparrow^\dagger(\mathbf{r}_i, \tau_i) \psi_\uparrow(\mathbf{r}_i, \tau_i) \psi_\downarrow^\dagger(\mathbf{r}_i, \tau_i) \psi_\downarrow(\mathbf{r}_i, \tau_i) \quad (2)$$

where $\psi(\mathbf{r}_i, t_i)$ and $\psi^\dagger(\mathbf{r}_i, t_i)$ are Grassmann variables at space-time point (\mathbf{r}_i, t_i) . The first part of the action corresponds to the kinetic energy, characterized by the bare Green's function G_0 which is obtained from the bare dispersion of the Hubbard model. The second term corresponds to the interaction characterized by the coulomb repulsion U , which is local.

The exact Green's function for this action is characterized by the self-energy Σ . In the frequency-momentum space, the relation between the bare Green's function and the exact Green's function G is given by the Dyson equation:

$$G(\mathbf{k}, \omega) = \frac{1}{G_0^{-1}(\mathbf{k}, \omega) - \Sigma(\mathbf{k}, \omega)} \quad (3)$$

The idea of DMFT is to relate the full lattice problem, with spatial dependence, to a single-site problem. The concept of the "cavity method" justifies this approach in the infinite-dimension limit where all the degrees of freedom are integrated out except for one central site as shown in Fig.(1(a)) and Fig.(1(b)) [9]. In the limit of $d \rightarrow \infty$, we rescale the hopping amplitude, $t_{ij} = \frac{t}{\sqrt{2d}}$, so that the kinetic energy and the interaction energy remain of the same order. The effective action S_{eff} is defined in the frequency domain by:

$$S_{eff} = - \int d\omega \sum_{\sigma} \psi_{\sigma}^{\dagger}(\omega) \mathcal{G}^{-1}(\omega) \psi_{\sigma}(\omega) + U \int_{\omega_1 + \omega_3 = \omega_2 + \omega_4} d\omega_1 d\omega_2 d\omega_3 d\omega_4 \psi_{\uparrow}^{\dagger}(\omega_1) \psi_{\uparrow}(\omega_2) \psi_{\downarrow}^{\dagger}(\omega_3) \psi_{\downarrow}(\omega_4). \quad (4)$$

Where, in the quadratic part of the impurity action, \mathcal{G} can be written on the Bethe lattice in terms of the lattice Green's function as [8–11, 86]:

$$\mathcal{G}^{-1}(i\omega_n) = i\omega_n + \mu - t^2 G(i\omega_n) \quad (5)$$

Eq.(5) is the self-consistency equation for the DMFT.

The Green's function from this action is $G(i\omega_n)$ which is then fed into the Eq.(5) until the dynamical mean-field, that is the bath Green's function, $\mathcal{G}(i\omega_n)$, is converged [9].

The key step of the DMFT algorithm is, given this effective action of the system, to find Green's function. There are two major types of methods to address this challenge: QMC methods based on sampling the partition function directly or Hamiltonian methods based on the discretization of the electron bath into a finite number of so-called bath sites. For the latter, the DMFT impurity problem can be described by the Anderson impurity model (AIM) or the single impurity Anderson model (SIAM) defined by the Hamiltonian:

$$H_{AIM} = U \hat{n}_{\downarrow} \hat{n}_{\uparrow} - \mu \sum_{\sigma} \hat{n}_{\sigma} + \sum_{j\sigma} \epsilon_j \hat{f}_{j,\sigma}^{\dagger} \hat{f}_{j,\sigma} + \sum_{j\sigma} V_j (\hat{c}_{\sigma}^{\dagger} \hat{f}_{j,\sigma} + h.c). \quad (6)$$

Here, $\hat{c}_{\sigma}^{\dagger}$ and \hat{c}_{σ} are creation and annihilation operators for impurity electrons, while $\hat{f}_{j\sigma}^{\dagger}$ and $\hat{f}_{j\sigma}$ are those of conduction electrons. The action of the Hamiltonian (6) can be written as that of Eq.(4), with \mathcal{G} as the non-interacting Anderson impurity model green's function, if the number of bath electrons goes to infinity. From now on, without specification, we consider single-particle quantities in real-time or frequency. The frequency ω , should be understood as $\omega + i\delta$. The connection between the lattice Hubbard model and the single impurity model is when we get the self-energy as:

$$\Sigma(\mathbf{k}, \omega) = \Sigma_{imp}(\omega) \quad (7)$$

This is fulfilled when we reach the DMFT self-consistency condition :

$$G(\mathbf{k}, \omega) = G_{imp}(\omega) \quad (8)$$

The hybridization and hopping of conduction electrons on a finite lattice is related to those of the continuum bath via the bare Green's function as[9–11],

$$\mathcal{G}^{-1}(i\omega_n) = i\omega_n + \mu - \Delta(i\omega_n) \quad (9)$$

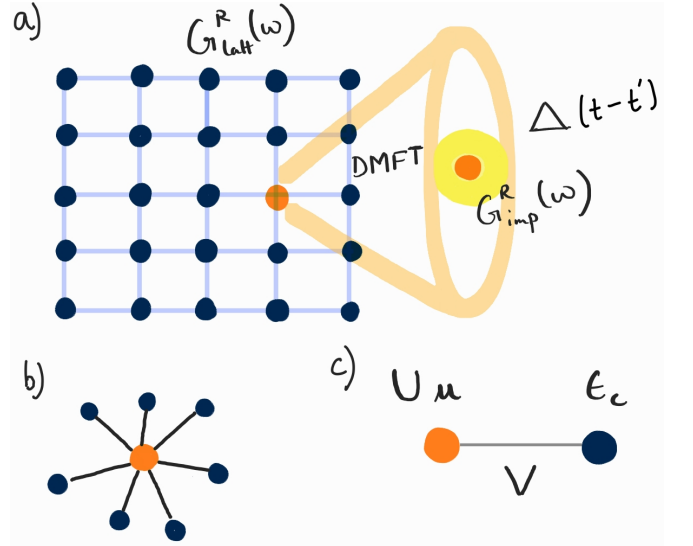


FIG. 1. (a) DMFT neglects spatial fluctuations around a single site and replaces the rest of the lattice with an effective mean-field subject to the self-consistency condition. (b) The non-interacting bath sites are connected to the central, interacting impurity site. (c) Minimal representation of two-site DMFT.

with

$$\Delta(i\omega_n) = \int_{-\infty}^{+\infty} d\omega \frac{1}{(i\omega_n - \omega)} \sum_{j\sigma} V_j^2 \delta(\omega - \epsilon_j). \quad (10)$$

This Hamiltonian formulation is more convenient for impurity solvers that are based on matrix diagonalization. Such solvers include exact diagonalization [87–89], numerical renormalization group [90, 91], and other more elaborate methods such as density matrix renormalization group and matrix product state[92, 93] and Fock tensor product state [94, 95].

A. Two site DMFT

The two-site representation of the SIAM [96] as shown in Fig.(1(c)) involves one fermionic site corresponding to the impurity and only one fermionic site corresponding to the bath. The SIAM Hamiltonian for one bath site is as follows.

$$H_{SIAM} = U \hat{n}_{1,\downarrow} \hat{n}_{1,\uparrow} - \mu \sum_{\sigma} \hat{n}_{1,\sigma} + \sum_{\sigma} \epsilon_c \hat{c}_{2,\sigma}^{\dagger} \hat{c}_{2,\sigma} + \sum_{\sigma} V (\hat{c}_{1,\sigma}^{\dagger} \hat{c}_{2,\sigma} + h.c) \quad (11)$$

Here, U is the on-site Hubbard interaction at the impurity site 1, and μ is the chemical potential that controls the electron filling. ϵ_c and V denotes the on-site energy of the non-interacting bath site 2 and the hybridization between the impurity and the bath site, respectively. For

a mapping of the DMFT to the two-site SIAM, the parameters ϵ_c and V are initially unknown and must be determined iteratively so that the two self-consistency conditions below are satisfied.

In the high-frequency limit, the self-energy of the impurity problem can be expanded in powers of $1/\omega$ [96]

$$\Sigma(\omega) = Un_c + \frac{U^2 n_c (1 - n_c)}{\omega} + \mathcal{O}(1/\omega^2) \quad (12)$$

where $n_c = n_{c\sigma}$ is the average occupancy of the impurity orbital:

$$n_c = \langle \hat{c}_\sigma^\dagger \hat{c}_\sigma \rangle = -\frac{1}{\pi} \int_{-\infty}^0 \text{Im} G_{imp}(\omega + i\delta) d\omega \quad (13)$$

Inserting the expansion (12) into (13), one finds the following expansion of the on-site lattice Green's function:

$$G(\omega) = \frac{1}{\omega} + \frac{t_0 - \mu + Un_c^2}{\omega^2} + \frac{M_2^{(0)} + \dots}{\omega^3} + \mathcal{O}(1/\omega^4) \quad (14)$$

Here $M_2^{(0)} = \Sigma_{j \neq i} t_{ij}^2 = \int dx x^2 \rho_0(x)$ is the variance of the non-interacting density of states (ρ_0).

The first condition is that the electron filling $n_{imp} = 2n_c$ of the impurity site can be identified with the filling $n = n_{j\downarrow} + n_{j\uparrow}$ of the lattice model, i.e.,

$$n_{imp} \equiv n \quad (15)$$

where the band filling is calculated via

$$n = -\frac{2}{\pi} \int_{-\infty}^0 \text{Im} G(\omega + i\delta) d\omega \quad (16)$$

with $G = G_{imp}$ and a broadening of δ .

Consider now the low-frequency limit, the self-energy of the impurity problem can be expanded in powers of ω ,

$$\Sigma(\omega) = a + b\omega + \mathcal{O}(\omega^2) \quad (17)$$

with a and b as constants. The quasi-particle weight is

$$\mathcal{Z} = \frac{1}{1 - b} = \left[1 - \frac{\text{dRe}[\Sigma_{imp}(\omega + i\delta)]}{\text{d}\omega} \Big|_{\omega=0} \right]^{-1} \quad (18)$$

Neglecting terms of order ω^2 , yields $G(\omega) = G^{(coh)}(\omega)$ for small ω where $G^{(coh)}(\omega)$ is the coherent part of the on-site Green's function [96]. Comparing the high-frequency expansions of the respective coherent Green's functions leads to the second self-consistency condition:

$$V^2 = \mathcal{Z} M_2^{(0)} = \mathcal{Z} \int_{-\infty}^{+\infty} d\epsilon \epsilon^2 \rho_0(\epsilon) \equiv \mathcal{Z} t^{*2}. \quad (19)$$

In Eq.(19), $M_2^{(0)}$ is the second moment of the non-interacting density of states, and the final equality follows from the semicircular density of states of the Bethe lattice [97].

Thereby, the original self-consistency condition is fulfilled at low frequencies up to $\mathcal{O}(\omega^2)$, by referring to

the weight, the center, and the variance of the coherent quasi-particle peak. Eq.(15) and Eq.(19) reformulate the DMFT self-consistency equation. Instead of requiring the self-energy as a function of frequency, it now involves two equations for fixing ϵ_c and V as these are the only parameters in the effective two-site model. This is much simplified compared to the full DMFT in which the Green's function for each frequency point from the lattice is mapped to that of the impurity.

III. METHODS AND PROCEDURE

After the formulation of the two sites DMFT, the next step is to transform the problem from fermionic operators into spin- $\frac{1}{2}$ operators for the quantum algorithms. The ground state of the Hamiltonian is obtained by the variational quantum eigensolver (VQE) and the Green's functions are then calculated via the Trotter-Suzuki approximation. With the Green's function, the quasi-particle weight can be calculated and the self-consistency equations can be solved. The procedure is repeated until the desired convergence of the quasi-particle weight is attained. We only consider the half-filled case in this study, so that the chemical potential can be fixed by hand exactly by explicitly enforcing the particle-hole symmetry. We explain the details of the above step in the following. The procedure largely follows that of Kreula *et al.* [30] and modified by Keen *et al.* [32]

A. Jordan-Wigner Transformation

We follow the standard Jordan-Wigner transformation to transform the fermionic creation and annihilation operators into spin operators for representation on a quantum computer [98]. In a two-site SIAM, a four-qubit system (excluding the ancilla qubit used for measurement) is required. The first two qubits encode the spin-down information for sites one and two, while the third and fourth qubits encode the corresponding information for the spin-up occupation. This process leads to the transformed operators [30]:

$$c_{1\downarrow}^\dagger = \sigma_1^- = \frac{X_1 - iY_1}{2} \quad (20)$$

$$c_{2\downarrow}^\dagger = Z_1 \sigma_2^- = \frac{Z_1(X_2 - iY_2)}{2} \quad (21)$$

$$c_{1\uparrow}^\dagger = Z_1 Z_2 \sigma_3^- = \frac{Z_1 Z_2 (X_3 - iY_3)}{2} \quad (22)$$

$$c_{2\uparrow}^\dagger = Z_1 Z_2 Z_3 \sigma_4^- = \frac{Z_1 Z_2 Z_3 (X_4 - iY_4)}{2} \quad (23)$$

Here, X_i, Y_i , or Z_i denote operators on the i^{th} qubit, while identity operators act on the remaining qubits. In this representation, the two-site SIAM Hamiltonian is

given by

$$\begin{aligned}
H_{SIAM} &= \frac{U}{4}(Z_1 Z_3 - Z_1 - Z_3) \\
&+ \frac{\mu}{2}(Z_1 + Z_3) - \frac{\epsilon_c}{2}(Z_2 + Z_4) \\
&+ \frac{V}{2}(X_1 X_2 + Y_1 Y_2 + X_3 X_4 + Y_3 Y_4). \quad (24)
\end{aligned}$$

VQE is employed to find the ground state of the Hamiltonian. Details about the variational wavefunction used are explained in the next section.

We use the first-order Trotter-Suzuki expansion of the time evolution operator with the ground state wavefunction to calculate the Green's function in real-time. The Trotter-Suzuki transformation is given as

$$\begin{aligned}
\hat{U}(t) &= e^{-iH_{AI}t} \\
&\sim (e^{-i\frac{V}{2}(X_1 X_2 + Y_1 Y_2)\Delta t} e^{-i\frac{V}{2}(X_3 X_4 + Y_3 Y_4)\Delta t} \\
&\times e^{-i\frac{U}{4}(Z_1 Z_3)\Delta t} e^{i\frac{U-2\mu}{4}(Z_1)\Delta t} e^{i\frac{U-2\mu}{4}(Z_3)\Delta t} \\
&\times e^{i\frac{\epsilon_c}{2}(Z_2)\Delta t} e^{i\frac{\epsilon_c}{2}(Z_4)\Delta t} + \mathcal{O}((\Delta t)^2))^N \quad (25)
\end{aligned}$$

where t is the total time, N is the number of time steps and $\Delta t = \frac{t}{N}$ [99–101].

We only focus on the case $\sigma = \downarrow$. As we only consider the paramagnetic solution of the DMFT, it does not break the spin rotational symmetry. The retarded zero temperature impurity Green's function in the time domain is given by

$$\begin{aligned}
G_{imp}^R(t) &= \theta(t)(G_{imp}^>(t) - G_{imp}^<(t)) \quad (26) \\
&= -i\theta(t)(\langle \hat{c}_{1\sigma}(t)\hat{c}_{1\sigma}^\dagger(0) \rangle - \langle \hat{c}_{1\sigma}^\dagger(0)\hat{c}_{1\sigma}(t) \rangle)
\end{aligned}$$

The above equation is recast into spin operators via the Jordan-Wigner transformation. The Green's functions $G^>$ and $G^<$ can be written in terms of the spin operators.

$$\begin{aligned}
G_{imp}^>(t) &= -\frac{i}{4}[\langle \hat{U}^\dagger(t)X_1\hat{U}(t)X_1 \rangle \\
&- i\langle \hat{U}^\dagger(t)X_1\hat{U}(t)Y_1 \rangle \\
&+ i\langle \hat{U}^\dagger(t)Y_1\hat{U}(t)X_1 \rangle \\
&+ \langle \hat{U}^\dagger(t)Y_1\hat{U}(t)Y_1 \rangle] \quad (27)
\end{aligned}$$

$$\begin{aligned}
G_{imp}^<(t) &= \frac{i}{4}[\langle X_1\hat{U}^\dagger(t)X_1\hat{U}(t) \rangle \\
&+ i\langle X_1\hat{U}^\dagger(t)Y_1\hat{U}(t) \rangle \\
&- i\langle Y_1\hat{U}^\dagger(t)X_1\hat{U}(t) \rangle \\
&+ \langle Y_1\hat{U}^\dagger(t)Y_1\hat{U}(t) \rangle] \quad (28)
\end{aligned}$$

After measuring the retarded impurity Green's function $G_{imp}(t)$ at each Trotter step, $iG_{imp}(t)$ is least-squares fitted on a classical computer. In the two-site DMFT, the interacting Green's function is a four-pole function, and, due to the presence of particle-hole symmetry, we have

$$iG_{imp}(t) = 2(\alpha_1 \cos(\omega_1 t) + \alpha_2 \cos(\omega_2 t)). \quad (29)$$

where $\alpha_2 = 0.5 - \alpha_1$ at half filling. Fourier transforming the above equation leads to

$$\begin{aligned}
G_{imp}^R(\omega + i\delta) &= \alpha_1 \left(\frac{1}{\omega + i\delta - \omega_1} + \frac{1}{\omega + i\delta + \omega_1} \right) \\
&+ \alpha_2 \left(\frac{1}{\omega + i\delta - \omega_2} + \frac{1}{\omega + i\delta + \omega_2} \right), \quad (30)
\end{aligned}$$

where δ is an artificial broadening parameter. As the self-consistency is reached, the optimal parameters are obtained, the Dyson equation is used to calculate the self-energy and, subsequently, the spectral function $A(\omega) = -\frac{1}{\pi} \text{Im}[G_{imp}(\omega + i\delta)]$.

A common practice for calculating the self-energy is to employ the Dyson equation in the frequency domain. Since $G_0(\omega)$ is given as the input of the impurity problem and $G_{imp}(\omega)$ is obtained by the above fitting procedure via Fourier transform. The self-energy can be seemingly easy to obtain by

$$\Sigma(\omega) = G_0^{-1}(\omega) - G_{imp}^{-1}(\omega) \quad (31)$$

where the bare Green's function is

$$G_0(\omega + i\delta) = \frac{1}{(\omega + i\delta) + \mu - V^2/(\omega + i\delta)} \quad (32)$$

Since the quasi-particle weight is given by the derivative of the real part of the self-energy at zero frequency, we need to solve the Eq.(31) at zero frequency. Unfortunately, it is not easy to calculate the self-energy accurately, as the number of states in the two-sites system is very limited, the subtraction of the two Green's functions in the Dyson equation is essentially a subtraction of a set of delta functions. This does not pose a serious issue when the bath is in the continuum and is actually done routinely in most numerical DMFT calculations [9]. However, the limited number of states available in the present problem makes the results highly sensitive to the choice of the damping parameter in the Fourier transform of Green's function from the real-time domain to the frequency domain. Strictly speaking, there is also a damping factor associated with time, however, the available time in the present calculation is always limited to a finite number.

A remedy has been proposed by Keen *et al.* in Ref. [32]. The idea is, instead of calculating the self-energy at zero energy by subtracting the inverse of the bath and the interacting Green's function at zero, to consider the sum over a window of energy. This clearly provides more stable and consistent results which are less dependent on the damping factors [32].

This is a viable method for achieving better stability in the iteration step of finding the self-consistent solution of the DMFT. As far as the two-site DMFT is concerned, this integration method is applicable. However, for more general settings such as the cases for multiple bath sites, the self-consistency is more involved. Instead of just the quasi-particle weight, the full self-energy needs to be obtained and the integration method cannot be readily generalized for those situations. Moreover, the integration

method also brings an additional parameter that cannot be fixed simply.

Therefore, it is desirable to have a method that has minimal dependence on arbitrary parameters, specifically the damping and the integration range, but is sufficiently stable for the iterative solution of the DMFT equations. We observe that the system is a finite-size cluster, therefore the self-energy of the two-site impurity problem is a two-pole function of the form [96],

$$\Sigma(\omega) = \gamma_0 + \frac{\gamma_1}{\omega - \omega_1^s} + \frac{\gamma_2}{\omega - \omega_2^s}. \quad (33)$$

The self-energy is completely determined by five parameters, γ_0 , γ_1 , γ_2 , ω_1^s and ω_2^s , where $\gamma_1 = \gamma_2$ and $\omega_1^s + \omega_2^s = 0$ at half filling. We can Fourier transform the self-energy back to the time domain with the explicit form of it. The functional form will be the same as that of the Green's function. Instead of calculating the self-energy in the frequency domain, we can use the Dyson equation in the time domain to calculate the self-energy. Both the inverse of the bath and interacting Green's function are well-behaved. The parameters, γ_0 , γ_1 , and γ_2 are then obtained by fitting the self-energy as the difference between the inverse of the bath and the interacting Green's functions in the time domain. After the fitting, the full self-energy is obtained and can be used to extract quasi-particle weight and any other physical quantities.

The self-energy obtained in this way has a minimal number of arbitrary parameters. The remaining arbitrary parameters are the upper limit of the time and the time step in the Trotter-Suzuki approximation, which are both intrinsic limitations of the quantum algorithm. Therefore, no additional arbitrary parameter is introduced except those limited by the quantum algorithm.

B. Flowchart

The hybrid quantum-classical simulation of the two-site DMFT consists of a few qubit digital quantum simulators to calculate the impurity Green's function and a classical feedback loop where the parameters of the two-site SIAM are updated [29]. The algorithm, depicted in Fig.(2), proceeds as follows:

1. Fix U and μ to the desired values in the SIAM and set the unknown parameters $\epsilon_c = 0$ for half-filling, and V to an initial guess.
2. Measure the interacting Green's function $iG_{imp}(t)$. This is done using single-qubit interferometry.
3. Fourier transform the impurity Green's function by fitting it according to Eq.(29).
4. Calculate the coefficients for the self-energy by using the Dyson equation in the time domain.
5. Measure the quasi-particle weight \mathcal{Z} by using the self energy.

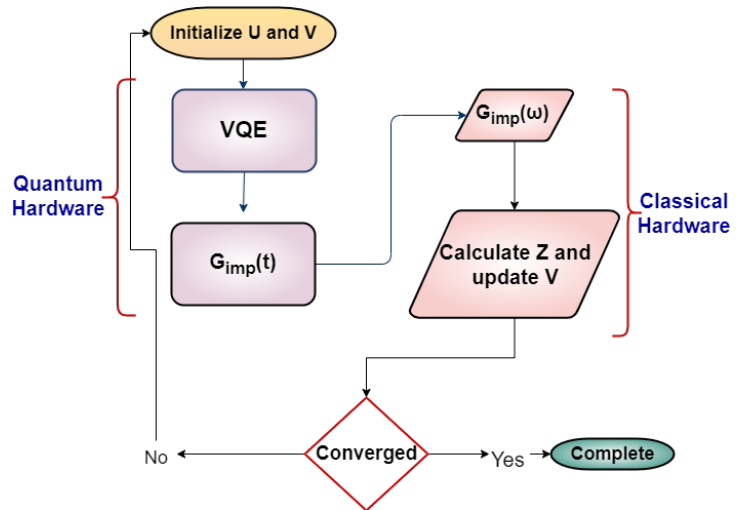


FIG. 2. Flowchart for the two-site DMFT calculation implemented on a hybrid quantum-classical system. For the half-filled case, the only external parameter is the Hubbard U . The iteration for the self-consistent solution for the quasi-particle weight \mathcal{Z} starts from a given U and an initial guess for V . With these values of U and V , the two sites impurity problem is solved by finding the ground state by the variational quantum eigensolver(VQE) and then the Green's function in real-time is obtained by propagating the ground state using the evolution operator $\exp(-iHt)$. The above procedure can be done in quantum hardware except for the minimization process for the VQE. Once the Green's function in real-time, $G(t)$, is obtained, we find the Fourier transformed Green's function $G(\omega)$ by a fitting procedure as explained in section III-A. With the $G(\omega)$, the quasi-particle weight, \mathcal{Z} , can be calculated by using Eq. 18. With the obtained \mathcal{Z} , we can update the hybridization V , using the relation $V = \sqrt{\mathcal{Z}}$. Then, the V is checked for convergence. The fitting process is done in the classical hardware.

6. Update the hopping parameter V .

7. Repeat steps 2-6 until the self-energy is converged.

IV. IMPLEMENTATION

A. Ground state Ansatz

The variational ansatz is prepared by a circuit with three CNOTs and eight single qubit rotations, see Fig.(3). The VQE then optimizes the single qubit rotation parameters to minimize the expectation value of the target Hamiltonian H_{SIAM} for given values of V, U, ϵ_c, μ to obtain the ground state of the system. We note that the choice of a variational state is not unique. Choosing an optimized variational ansatz has been an important but largely unsolved problem, even in the context of the classical variational method as routinely performed by VMC. We do not attempt to find the 'best' possible wave function in the present study [29, 30].

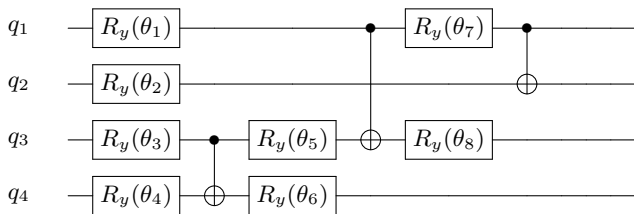
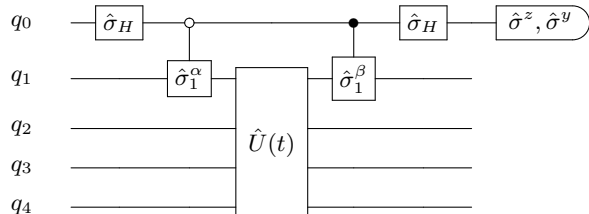


FIG. 3. Quantum circuit for the ground state ansatz.

FIG. 4. Quantum circuit for measuring the individual components of $G_{imp}(t)$. $\hat{U}(t)$ is composed of quantum gates. $\hat{\sigma}^H$ is the Hadamard gate. $\hat{\sigma}_1^\alpha$ and $\hat{\sigma}_1^\beta$ can be X_1 and Y_1 according to the components in Eqs. (27) and (28) that we measure.

The ‘best’ wavefunction is model and even parameter-dependent [102]. We fix the functional form of the wavefunction for the entire range of on-site interaction strength, which likely is not the ‘best’ optimized wavefunction.

B. Retarded Impurity Green’s Function

The measurement of the impurity Green’s function $G_{imp}(t)$ is done by single-qubit Ramsey interferometer, shown in Fig. (4) [30, 103], which is used in the more general non-equilibrium case. An ancilla qubit is introduced in addition to the ‘system’ qubits, raising the total number of qubits needed to implement the two-site DMFT scheme to five.

V. RESULTS

We start by examining the procedure of obtaining the impurity Green’s function in the DMFT routine. Fig.(5) shows the impurity Green’s function in the time domain for two different sets of parameters, $V = t$ (top) and $V = 0$ (bottom) with $U = 8t$ for both cases. We superimpose the data in Fig.(5) to the fit obtained according to the exact result of Eq.(29). The calculated Green’s function data is obtained with a modest number of time steps (18 in this case).

The impurity Green’s function in the frequency domain $G_{imp}(\omega)$ obtained after self-consistency is achieved, extracted from the fit parameters following Eq.(30). Some of the additional results calculated from the ground state

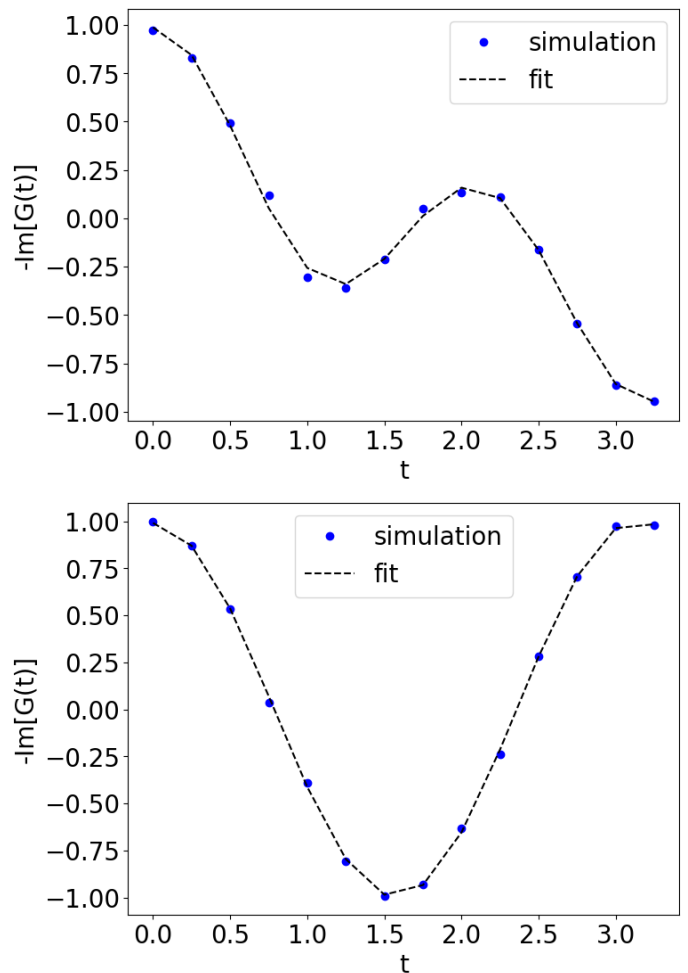


FIG. 5. Top: Impurity Green’s function for $U = 8t$ and $V = t$. The parameters for the fit shown are $\alpha_1 = 0.002$, $\alpha_2 = 0.496$, $\omega_1 = 3.874$, $\omega_2 = 1.999$. Bottom: Impurity Green’s function for $U = 8t$ and $V = 0$. The parameters for the fit shown are $\alpha_1 = 0.295$, $\alpha_2 = 0.055$, $\omega_1 = 3.143$, and $\omega_2 = 5.014$. We fit the impurity Green’s function to Eq. (29)

obtained from the VQE are presented in Appendix A.

We obtain the energies ω_1 and ω_2 from fitting the Green’s function to Eq.(29) for half-filling. We then Fourier transform the impurity Green’s Function according to Eq.(30) to the frequency domain. We use the Dyson equation to calculate the self-energy in the frequency domain from Eq.(31). We obtain the parameters γ_0 , γ_1 , and γ_2 , by fitting the self-energy to Eq.(33). Fig.(6) shows the quasi-particle weight at self-consistency using Eq(18) for U values ranging from 0.01 to 10.0. All of the data in Fig.(6) was calculated on a classical computer.

In addition to the quasi-particle weight, another quantity that may indicate a phase transition is the entanglement entropy. It has been tested extensively on fermionic lattice models that the entanglement, combined with the finite size scaling, can be used to determine the critical

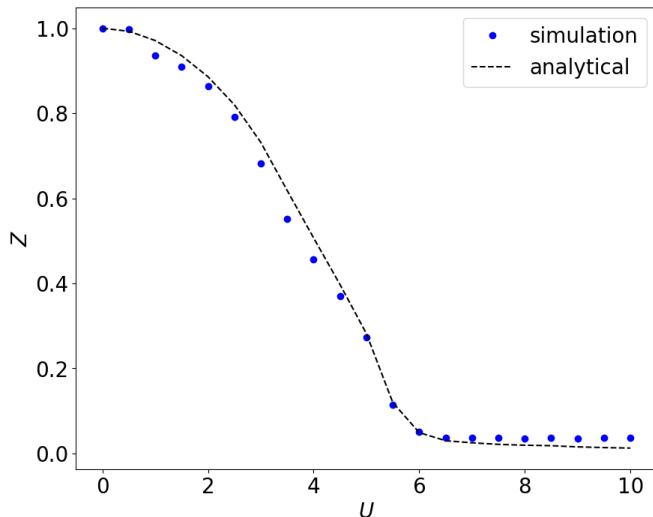


FIG. 6. Quasi-particle weight at self-consistency as a function of U from self-energy calculation using Eq.(18). The analytical expression of the quasi-particle weight for the half-filling case is obtained from Eq.(31) of Potthoff [96]

point [104–106]. The idea of using entanglement entropy within DMFT has not previously been explored in detail. There is a clear choice of dividing the system into two parts here, as the effective problem that is being solved in DMFT is the SIAM. We can define the entanglement entropy between the impurity site and the bath sites naturally, that is

$$E_v = -Tr[\rho_{imp} \log(\rho_{imp})], \quad (34)$$

where ρ_{imp} is the reduced density matrix for the impurity site. It is obtained by tracing out the degree of freedom from the bath sites in the density matrix for the ground state ($|GS\rangle$). That is $\rho_{imp} = Tr_{bath}(\rho)$, where $\rho = |GS\rangle\langle GS|$. The behavior of the local entanglement for the half-filling case is shown in Fig.(7).

In the large U limit, $|U| \rightarrow \infty$, all sites are singly occupied, one gets $E_v(|U| \rightarrow \infty) = 0$.

For finite $|U|$, the hopping process enhances E_v , and hence reaches its maximum value, 2 at $U = 0$.

VI. CLASSIFICATION USING QUANTUM MACHINE LEARNING

In the previous section, we obtain the Green’s function of the Hubbard model under the DMFT approximation. In addition, we also have the wavefunction for the effective impurity problem from the DMFT, which contains all the information about the system. Instead of directly calculating an “order parameter”, we try to identify the different phases from the wavefunction. It is worthwhile to note that, unlike the DMFT with a continuum bath, the system here is a finite-size system, therefore, there is no true phase transition as that of the thermodynamic

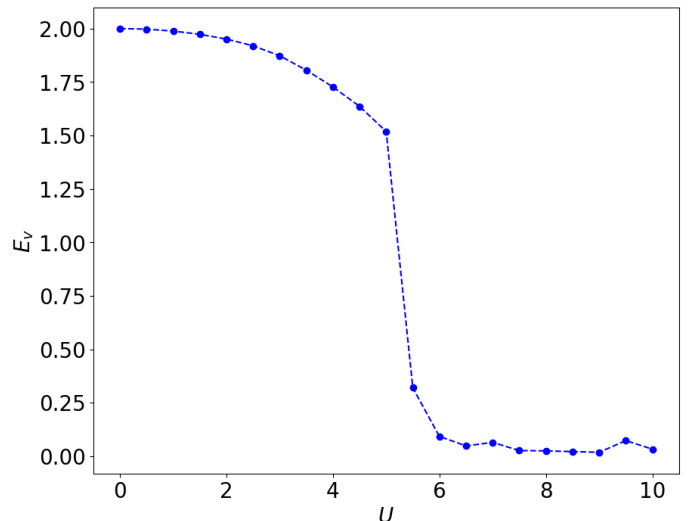


FIG. 7. Local entanglement E_v of the two-site SIAM at half-filling versus the on-site coupling U calculated using Eq.(34).

limit. Notwithstanding this noteworthy deficit, it has been shown that classical ML methods can locate phase transitions as well as crossovers rather accurately from finite-size classical and even quantum systems [34, 107].

A. QML as a Classifier of Wavefunctions

Since our data is inherently quantum, it is natural to involve a QML approach to try to identify the phase transition. In the present study, we focus only on supervised learning. Exactly as that in classical ML, the first step is to label input objects [107]. The input object here is the wavefunction, and the label is whether the wavefunction corresponds to a metal or insulator.

The major conceptual difference between the QML and the classical ML is in the input data and the function which generates the output label. A popular choice for classical ML is to treat the input data as an array of numbers, and the function is usually chosen as a form of neural network. For supervised learning, a data set consists of input objects, and their corresponding labels are then used to optimize the parameters in the neural network during the training.

Most applications of QML are focused on using classical datasets [108]. It is possible to cast the wavefunction expressed as a classical vector into quantum data. This is precisely what needs to be done using a quantum classifier for classical data, such as to identify classical images. For the present study, the input is wavefunctions from the converged DMFT solution, a genuinely quantum dataset, represented in quantum circuits from the VQE.

B. Implementation of the QCNN to Classify the Wavefunctions from the DMFT

Our objective is to showcase the effectiveness of the QCNN in identifying wavefunctions at different phases. From the converged DMFT solution, we obtain the input wavefunction, and the output label determines whether the wavefunction corresponds to a metal or an insulator.

The quantum neural network [108, 109] is a direct conceptual generalization of the classical neural network; the main difference is that the activation functions [108, 110, 111] are replaced by quantum gates and the input and output are replaced by quantum states instead of an array of classical variables. The quantum neural network we employed in the present study is denoted as QCNN [83]. A QCNN primarily consists of two distinct layer types: the pooling layer and the convolution layer. The pooling layer reduces the number of degrees of freedom and can be substituted by multi-qubit gates, the CNOT gate being the simplest option [83]. On the other hand, the convolution layer in a conventional CNN can be substituted by multi-qubit quantum gates among adjacent qubits.

The QCNN is constructed using an alternating sequence of convolutional and pooling layers until the number of pooling layers is reduced to a single qubit. The goal is for the QCNN to extract important information from the input quantum data and correctly identify the “phase” of each wavefunction, specifically for the detection of the quantum critical point of the SIAM. We train the QCNN in a supervised environment, where the correct phase identification for each data point is already known. For a given on-site potential U , we have either a metallic or Mott-insulator phase. The system is in a metallic phase below 6 and a Mott-insulator phase above 6 when U is in the $[0.0-10.0]$ range. We revisit the phase transition at $U = 6$. The reader may refer to Appendix B for the details of the QCNN circuit.

VII. CLASSIFIER RESULTS USING A QCNN

The QCNN was trained using two different selections of training data. 200 data points are generated for different U uniformly distributed over $0 < U \leq 10$. In the first set, the QCNN was trained by randomly selecting 80% of the wavefunctions with labels to designate their corresponding phases as the training data set. In the second set, only the data points corresponding to small and large on-site potential, U were used for training. The label for the metallic phase was defined as -1 , while the Mott insulating phase was defined as $+1$. To benchmark the accuracy of the predictions, the output was bound to -1 if the QCNN output measurement was smaller than 0 and similarly bound to $+1$ if the measurement was greater than 0.

A. Training QCNN with data for randomly picked data for $0.0 < U \leq 10.0$

We evaluate the performance of our trained QCNN by using the remaining 20% of available samples as a benchmark and track the loss and accuracy during each iteration of the training process. We plot the loss and accuracy as a function of epoch in Fig.(8). The accuracy is calculated by taking the mean of the tensor which is obtained after checking element-wise equality between the true labels and the predictions. We find the loss from calculating the mean of squares of errors between the true labels and the predictions [108]. It is defined as :

$$L(f(x), y) = \frac{(f(x) - y)^2}{N} \quad (35)$$

where y are the true labels, x are the input feature vectors which are wavefunctions, and $f(x)$ are the output predictions. N is the total number of input samples.

By randomly selecting wavefunctions for training, our QCNN is able to learn from the entire dataset, including samples with values of U both close and far from the quantum critical point. This enables the QCNN to become familiar with the wavefunctions and provide accurate predictions for the trained data. We achieve an accuracy of approximately 75% for both training and testing data, demonstrating that randomized training data allows the QCNN to adjust to variations in wavefunctions during training and generalize well to testing data. The QCNN exhibits the ability to predict the phase of wavefunctions, and we observe the training process through the loss values of the network. Despite the high loss values, we can visualize the QCNN’s training phase and observe its improvement in making correct predictions for the phase corresponding to the wavefunctions. In Fig. (9) we plot the average value of the predicted label as a function of U . We average over 10 data points to find the average label, we find that the label passes through zero around $U = 6$.

B. Training QCNN with data for $4.0 \leq U$ and $U \geq 7.0$

After considering the aforementioned findings, we opted to assess the performance of the QCNN using selected training and testing data. During training, we used wavefunctions that had U values below 4.0 and above 7.0, while the test data were within the range of $[4.0-7.0]$. This approach allowed us to determine how effectively the QCNN can classify data close to the known quantum critical point ($U = 6.0$) after training it with data away from it. During training, we obtained an accuracy rate of approximately 75 – 80%, which is not surprising given that the two sets of data with very large and very small values of U are quite different from each other.

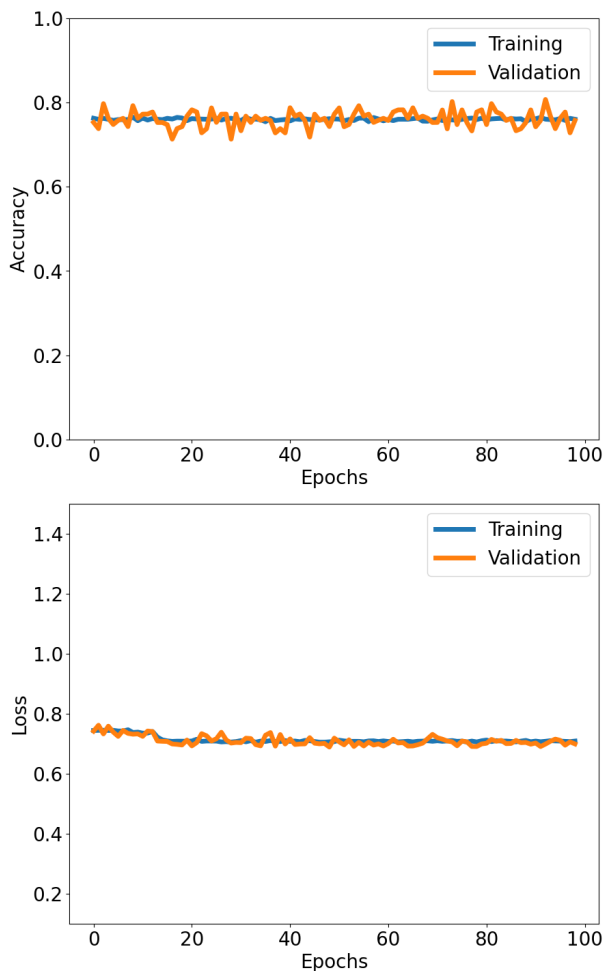


FIG. 8. Accuracy and Loss for the training and validation data set for the QCNN as a function of the number of epochs. Accuracy is the mean of the tensor calculated after checking element-wise equality between the true and predicted labels. Loss is the mean-squared error between the true and predicted labels calculated using Eq.(35).

We present the results in Fig.(10) and Fig.(11). We observed that the testing data consistently exhibited a lower accuracy rate than a randomized dataset. The QCNN is capable of classifying data points that are far from the quantum critical point. However, as we approached the putative quantum phase transition, the network faced greater difficulty with predictions. The average predicted label shows the crossing from negative to positive values for U between 5 and 6. The unfamiliarity with data points in this range hindered the accuracy of the testing data. The loss showed only slight changes during the training phase compared to using randomized data, and although we still observed a decrease, it was minimal. This indicates that the QCNN does not have much room for improvement when the testing data are isolated from the quantum critical point.

The exclusive use of high and low values of U during QCNN training has important implications for the iden-

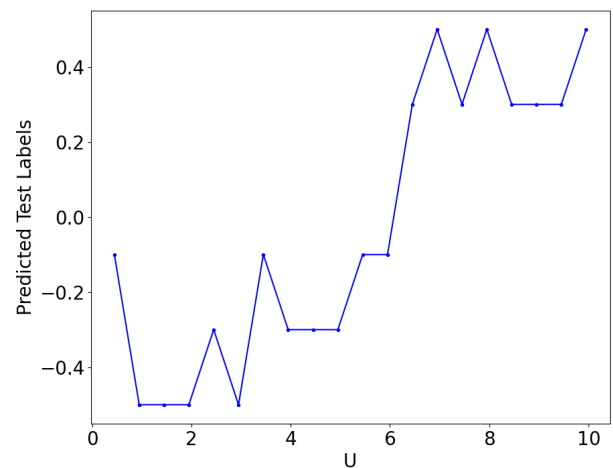


FIG. 9. Predicted test labels vs U . The predicted labels show a jump from a negative to a positive value around $U = 6.0$.

tification of quantum critical points. In classical ML, a common technique for detecting phase transitions involves training a supervised model (e.g., a CNN) using control parameters (such as temperature in thermal transitions or external parameters in quantum phase transitions) away from the hypothesized critical point. Our findings indicate that the QCNN can also achieve high accuracy by training on data outside of the hypothesized critical point to predict phases near the critical point [112]. Although the predicted label is clearly worse than the case for which the training data span the entire range of U . Nevertheless, the average predicted label still indicates that the quantum phase transition happens around $5 \leq U \leq 6$.

VIII. DISCUSSION

In this work, we present a hybrid quantum-classical algorithm for calculating the phase transition of the Hubbard model under the DMFT approximation. From a practical standpoint, the primary concern is addressing the noise generated by the deep circuit in the Trotter approximation, which affects phase estimation. We did not include the contributions from noise and dissipation in the present study. Recent proposals, in particular, the variational quantum simulation may provide a solution for this problem [113, 114]. The major difficulty of the method from a theoretical point of view is how to properly interpret the DMFT approximation realized in a very limited system size for the bath. If the bath is restricted to just one or a handful of sites, it may not be clear whether employing the formulation that presumes a continuous distribution of bath sites is either numerically feasible or physically meaningful.

The key quantity for the DMFT, particularly in the two-site approximation, is the quasi-particle weight. The quasi-particle weight can be defined as the measure of

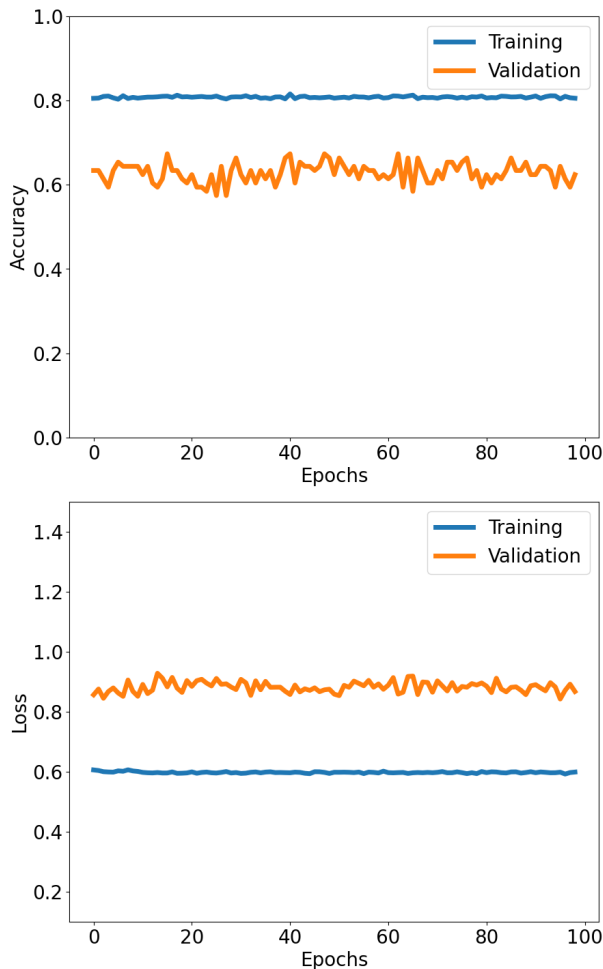


FIG. 10. Accuracy and Loss for the training and validation data set the QCNN as a function of the number of epochs. Accuracy is the mean of the tensor calculated after checking element-wise equality between the true and predicted labels. Loss is the mean-squared error between the true and predicted labels calculated using Eq.(35).

damping experienced by the quasi-particle at the Fermi level. It is usually calculated using the relation $\mathcal{Z} = (1 - (\partial \text{Re}(\Sigma(\omega)) / \partial \omega)|_{\omega = \theta})^{-1}$. However, the calculation of self-energy is problematic for a small number of bath sites. This is due to the challenge encountered in solving the Dyson equation for the self-energy $\Sigma(\omega) = G_0^{-1}(\omega) - G_{imp}^{-1}(\omega)$. The retarded Green's function is sensitive to the choice of the imaginary part included in the Fourier transform from time to frequency domains. While this may hold true in general, it is often not a significant factor for systems with a continuous bath - i.e., an infinite number of bath sites. In such systems, the choice of imaginary part typically does not play a substantial impact on the results, as they remain consistent across a range of choices. The focus of the imaginary part is how to distribute the few delta functions for a limited number of sites [96]. The self-energy obtained from the subtraction of the inverse of the full impurity

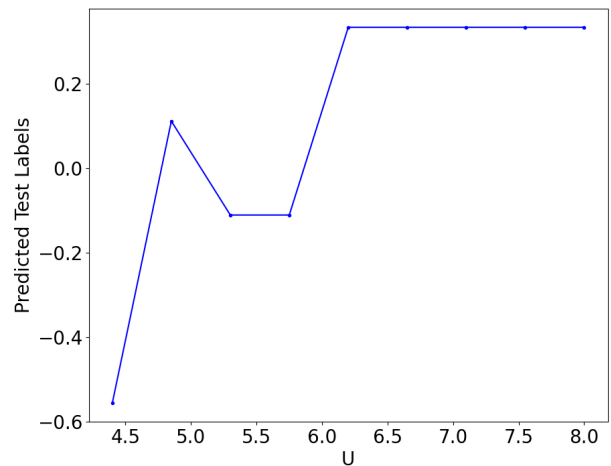


FIG. 11. Predicted test labels vs U . The predicted labels are hovering around zero for $5.0 \leq U \leq 6.0$.

Green's function from the inverse of the bare impurity Green's function cannot be estimated very accurately.

One method suggested is to replace the calculation of \mathcal{Z} from the Dyson equation at the Fermi energy with an averaging of the integration over an energy window centered around the Fermi level [32]. In a way, this approach shifts the problem from selecting the imaginary component in the frequency domain to selecting the integration range over an energy window around the Fermi level. Despite the somewhat arbitrary choice of this range of integration, this method has demonstrated good results [32].

In contrast to many other classical methods used for solving impurity problems, the impurity Green's function obtained through the VQE and Suzuki-Trotter approximation is expressed in real-time and the computation is limited to 'zero temperature'. This is an inherent advantage of this hybrid quantum-classical approach compared to conventional Monte Carlo-based approaches. This allows us to estimate the self-energy directly from the difference of the inverse of the interacting Green's function and the bath Green's function without going to the frequency space. The inverse of Green's function is more well-behaved and less prone to error in numerical calculations.

This approach of calculating the quasi-particle weight directly in the time domain not only avoids the possible ambiguity of choosing the windows of integration but is also more adaptable to a bath with multiple sites. This aligns more broadly with the objective of using hybrid quantum-classical algorithms. The advantage of this approach lies in the fact that we have the information for the self-energy for the full range of the data in the time domain. All the coefficients in the self-energy are calculated and in principle, a full DMFT can be used instead of just the single bath site approximation. In practice, calculations with a large number of bath sites may remain challenging in the near future due to the possibility of

increasing errors with larger system sizes. Nevertheless, the formulation presented here can easily be generalized to calculations with many bath sites.

Besides presenting a modification of the hybrid quantum-classical algorithm for the DMFT, we also tested a new quantity that has not been explored extensively in the context of DMFT [115]. Conventional DMFT is almost always being studied at a finite temperature, that may be rather low, but almost never at a true zero temperature for the Hubbard model. This is down to the fact that most existing methods for solving the impurity problems are practically feasible at low though non-zero temperatures. As the wavefunction is explicitly calculated, it is technically at the zero temperature and thus we can meaningfully define the entanglement entropy. The use of entanglement entropy as a witness to phase transition has been studied over the past two decades [116–118]. The general feature is that the entanglement entropy increase as the system is tuned close to a phase transition [104]. In the case of the half-filled Hubbard model in the two-site DMFT approach, it is observed that the entanglement entropy reaches its maximum value in the non-interacting limit, but gradually decreases until it saturates once the system enters the Mott insulating phase. A physical interpretation is that in the Mott insulating phase, the bath and the impurity are essentially decoupled, which minimizes the entanglement entropy between them.

For the present problem, the entanglement entropy may not provide much additional insight. However, there are important problems in condensed matter physics for which there is no obvious order parameter. This has been widely discussed in the context of some heavy fermion materials [119]. A method that can detect a putative transition without explicitly constructing an order parameter could be a useful technique.

For capturing the phase transition, we also elaborated on the application of a QML approach to identify phase transitions. The use of ML to locate phase transitions has been well-studied. However, using it for the quantum models requires some manipulations of the data, for example, the wavefunctions from exact diagonalization or the Feynman path integral from QMC are inherent quantum data represented in a classical dataset. Various approaches have been proposed and they are quite successful in finding phase transition [107]. Since the data from the VQE is true quantum data, it is natural to use QML. The data can be fed into the quantum classifiers without further manipulation of the data. This is an obvious advantage compared to using the classical ML approach for quantum data. The calculations done here utilizing the wavefunction derived from DMFT’s converged solution show promising although imperfect results.

Since using the ML approach to study phase transitions doesn’t require an explicit order parameter, this is advantageous in dealing with crossover problems, where there may not be an explicit order parameter or when the order parameter is unknown. One of them is the

crossover between the Fermi liquid and the marginal Fermi liquid [120–122]. A thorough study of the entanglement entropy may provide more insight into this crossover. Perhaps the major difficulty in studying phase transitions using NISQ computers is the rather limited system size. It’s reasonable to imagine that even if one can figure out and calculate an order parameter, a proper finite size scaling as done in conventional numerical simulations may remain out of reach. An ML-based approach could somehow bypass such difficulties and interpret the finite-size results directly.

IX. CONCLUSION

In summary, we provide a complete workflow for using NISQ to study phase transitions of strongly correlated systems in the thermodynamic limit using the dynamical mean field theory (DMFT). We devise a modification of the hybrid quantum-classical method to solve the DMFT using quantum hardware. Our modification provides results without arbitrary choices of parameters in estimating the quasi-particle weight. More importantly, it can be readily generalized for the DMFT with multiple bath sites. With the ground state wavefunction from DMFT, we proposed two approaches to capture phase transitions. The first one is based on calculating the entanglement entropy between the bath sites and the impurity sites. The second one is based on using the wavefunction from the converged solution of DMFT. We believe that there are many exciting prospects for these two approaches which have been enabled by the advance of quantum hardware.

X. ACKNOWLEDGMENT

This manuscript is based on work supported by NSF DMR-1728457. This work used high-performance computational resources provided by the Louisiana Optical Network Initiative (<http://www.loni.org>) and HPC@LSU computing. HFF is supported by the National Science Foundation under Grant No. PHY-2014023. H.T. is supported by NSF DMR-1944974 grant. JM is supported by the US Department of Energy, Office of Science, Office of Basic Energy Sciences, under Award Number DE-SC0017861.

Appendix A: Additional Results obtained for the Model

Fig.(12) shows the impurity Green’s function in the frequency domain. Analytically the exact expression for the impurity Green’s function for two-site SIAM for the half-filled case is obtained from Eq.(10) of Potthoff [96] and then we apply the Dyson equation using Eq.(30) from Potthoff [96]. Fig.(13) displays the self-energy of the sys-

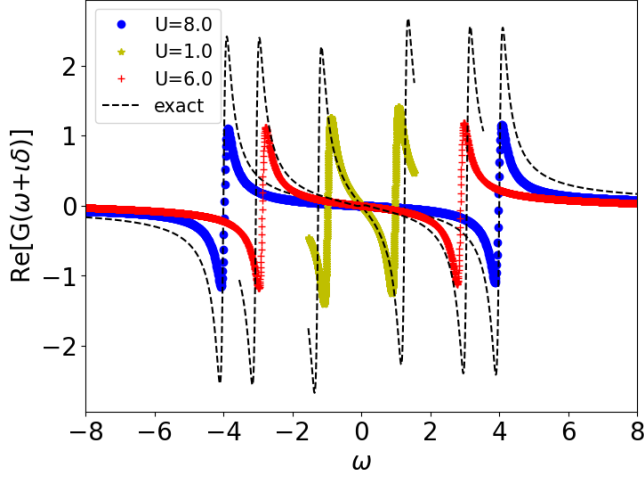


FIG. 12. The impurity Green's function with different U values and $V = 0$ in the frequency domain. Analytically the exact expression for the impurity Green's function is obtained from Eq. (10) of Potthoff [96]

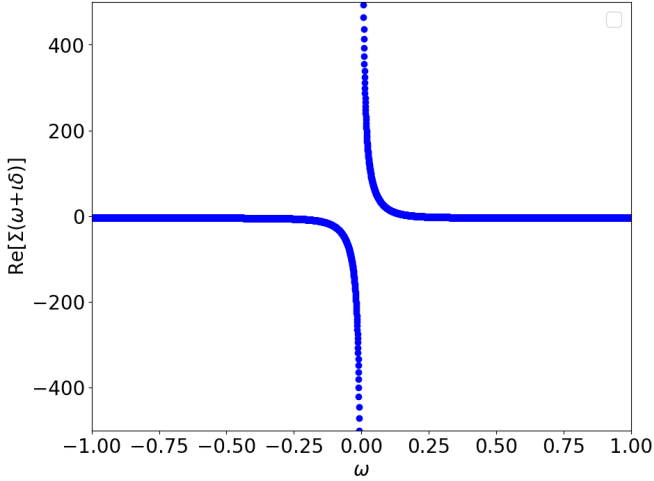


FIG. 13. The real part of the self-energy with $U = 8t$, $V = 0$, and a broadening of $\delta = 0.1$

tem at self-consistency, calculated using the Dyson equation Eq.(31).

Fig.(14) shows the spectral function, $A(\omega) =$

$-\frac{1}{\pi} \text{Im}[G_{imp}(\omega + i\delta)]$ obtained from the Green's function for both the simulation and the exact result. The Trotter error gives rise to the noise

that results in shifts in the fit frequencies ω_1 and ω_2 .

Appendix B: QCNN Circuit

QCNN consists of two main elements, the pooling layer, and the convolution layers, shown in Fig.(17) [83]. To achieve the pooling, we employ a pooling unit that combines two qubits into one qubit, as shown in Fig.(16).

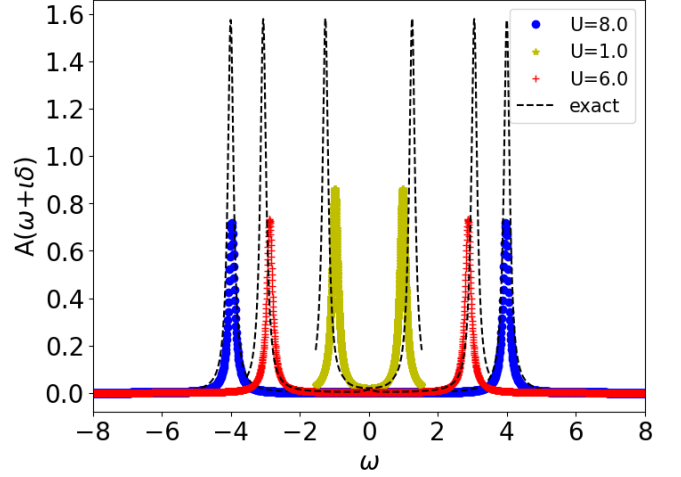


FIG. 14. The calculated spectral function from the Green's function with different U values, and $V = 0$, and a broadening of $\delta = 0.1$ for both the simulation and exact result.

The pooling unit includes local rotation gates on each qubit, followed by a controlled X-gate and the inverse rotation on the controlled bit. There are six parameters in each pooling unit.

The convolutional layer is made up of multiple two-qubit convolution units as shown in Fig.(15). A convolution unit consists of local rotation gates on each qubit, sandwiched between the ZZ coupling gates between the two qubits. There are 15 parameters for each convolutional unit between two qubits.

We implement the QCNN using Cirq and train it using the TensorFlow Quantum package [123].

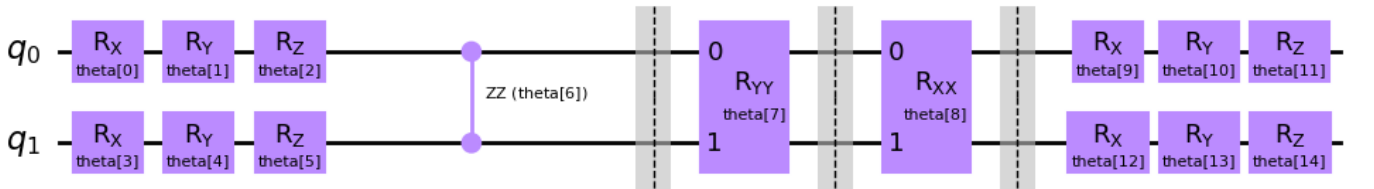


FIG. 15. Convolution between two qubits. A convolutional layer of N qubits is composed of $N/2$ convolutional units acting on the qubits. $x[0], x[1], \dots, x[14]$ are the parameters.

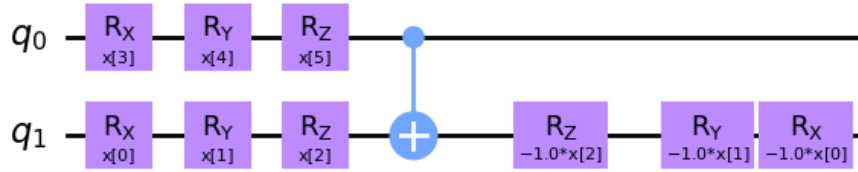


FIG. 16. Pooling between two qubits. A pooling layer from N qubits to $N/2$ qubits is composed of $N/2$ of pooling units. $x[0], x[1], \dots, x[5]$ are the parameters.

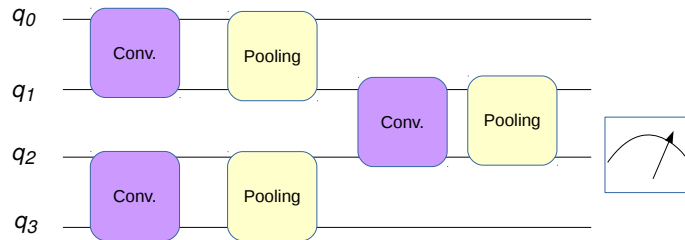


FIG. 17. The QCNN circuit for 4 qubits, two convolutional (Conv.) units act on the pairs of qubits. A pooling unit that reduces the 4 input qubits into 2 output qubits. Another layer of convolutional units on the pair of qubits and the pair of qubits is then fed into another pooling unit with one output qubit. The qubit from the last pooling unit is measured. Note that the parameters in each convolutional unit can be different from the others, and so does the pooling unit.

-
- [1] C. Varma, Z. Nussinov, and W. van Saarloos, *Phys. Rep.* **361**, 267–417 (2002).
- [2] L. Savary and L. Balents, *Rep. Prog. Phys.* **80**, 016502 (2016).
- [3] G. R. Stewart, *Rev. Mod. Phys.* **56**, 755 (1984).
- [4] C. Proust and L. Taillefer, *Annu. Rev. Condens. Matter Phys.* **10**, 409 (2019).
- [5] C. M. Varma, *Rev. Mod. Phys.* **92**, 031001 (2020).
- [6] J. Kanamori, *Prog. Theor. Exp. Phys.* **30**, 275 (1963).
- [7] J. Hubbard, *Proc. Math. Phys. Eng. Sci.* **276**, 238 (1963).
- [8] A. Georges and G. Kotliar, *Phys. Rev. B* **45**, 6479 (1992).
- [9] A. Georges, G. Kotliar, W. Krauth, and M. J. Rozenberg, *Rev. Mod. Phys.* **68**, 13 (1996).
- [10] E. Müller-Hartmann, *Z. Phys. B* **76**, 211 (1989).
- [11] E. Müller-Hartmann, *Z. Phys. B* **74**, 507 (1989).
- [12] W. Metzner and D. Vollhardt, *Phys. Rev. Lett.* **62**, 324 (1989).
- [13] M. Jarrell, *Phys. Rev. Lett.* **69**, 168 (1992).
- [14] A. Toschi, A. A. Katanin, and K. Held, *Phys. Rev. B* **75**, 045118 (2007).
- [15] A. N. Rubtsov, M. I. Katsnelson, A. I. Lichtenstein, and A. Georges, *Phys. Rev. B* **79**, 045133 (2009).
- [16] H. F. Fotso, K.-M. Tam, and J. Moreno, *Quantum Sci. Technol.* **7** (2020).
- [17] C. Slezak, M. Jarrell, T. Maier, and J. Deisz, *J. Condens. Matter Phys.* **21**, 435604 (2009).
- [18] J. P. Hague, M. Jarrell, and T. C. Schulthess, *Phys. Rev. B* **69**, 165113 (2004).
- [19] G. Rohringer, H. Hafermann, A. Toschi, A. A. Katanin, A. E. Antipov, M. I. Katsnelson, A. I. Lichtenstein, A. N. Rubtsov, and K. Held, *Rev. Mod. Phys.* **90**, 025003 (2018).
- [20] M. H. Hettler, M. Mukherjee, M. Jarrell, and H. R. Krishnamurthy, *Phys. Rev. B* **61**, 12739 (2000).
- [21] H. Fotso, S. Yang, K. Chen, S. Pathak, J. Moreno, M. Jarrell, K. Mikelsons, E. Khatami, and D. Galanakis, “Dynamical cluster approximation,” in *Strongly Correlated Systems: Theoretical Methods*, edited by A. Avella and F. Mancini (Springer Berlin Heidelberg, Berlin, Heidelberg, 2012) pp. 271–302.
- [22] G. Biroli and G. Kotliar, *Phys. Rev. B* **65**, 155112 (2002).
- [23] L.-F. Arsenault, A. Lopez-Bezanilla, O. A. von Lilienfeld, and A. J. Millis, *Phys. Rev. B* **90**, 155136 (2014).
- [24] J. B. Rigo and A. K. Mitchell, *Phys. Rev. B* **101**, 241105 (2020).
- [25] E. Sheridan, C. Rhodes, F. Jamet, I. Rungger, and C. Weber, *Phys. Rev. B* **104**, 205120 (2021).
- [26] N. Walker, S. Kellar, Y. Zhang, K.-M. Tam, and J. Moreno, *Crystals* **12** (2022).
- [27] E. J. Sturm, M. R. Carbone, D. Lu, A. Weichselbaum, and R. M. Konik, *Phys. Rev. B* **103**, 245118 (2021).
- [28] B. Bauer, D. Wecker, A. J. Millis, M. B. Hastings, and M. Troyer, *Phys. Rev. X* **6**, 031045 (2016).
- [29] T. Keen, T. Maier, S. Johnston, and P. Lougovski, *Quantum Sci. Technol.* **5**, 035001 (2020).
- [30] J. M. Kreula, L. García-Álvarez, L. Lamata, S. R. Clark, E. Solano, and D. Jaksch, *EPJ Quantum Technol.* **3**, 1 (2016).
- [31] I. Rungger, N. Fitzpatrick, H. Chen, C. H. Alderete, H. Apel, A. Cowtan, A. Patterson, D. M. Ramo, Y. Zhu, N. H. Nguyen, E. Grant, S. Chretien, L. Wossnig, N. M. Linke, and R. Duncan, “Dynamical mean field theory algorithm and experiment on quantum computers,” (2020), arXiv:1910.04735 [quant-ph].
- [32] T. Keen, T. Maier, S. Johnston, and P. Lougovski, *Quantum Sci. Technol.* **5**, 035001 (2020).
- [33] S. Johnston, E. Khatami, and R. Scalettar, *Carbon Trends* **9**, 100231 (2022).
- [34] L. Wang, *Phys. Rev. B* **94**, 195105 (2016).
- [35] E. P. L. van Nieuwenburg, Y.-H. Liu, and S. D. Huber, *Nat. Phys.* **13**, 435 (2017).
- [36] A. Baul, N. Walker, J. Moreno, and K.-M. Tam, *Phys. Rev. E* **107**, 045301 (2023).
- [37] X.-Y. Dong, F. Pollmann, and X.-F. Zhang, *Phys. Rev. B* **99**, 121104 (2019).
- [38] G. Cassella, H. Sutterud, S. Azadi, N. D. Drummond, D. Pfau, J. S. Spencer, and W. M. C. Foulkes, *Phys. Rev. Lett.* **130**, 036401 (2023).
- [39] S. J. Wetzel, *Phys. Rev. E* **96**, 022140 (2017).
- [40] W. Hu, R. R. P. Singh, and R. T. Scalettar, *Phys. Rev. E* **95**, 062122 (2017).
- [41] L. Wang, *Phys. Rev. B* **94**, 195105 (2016).
- [42] N. Walker, K.-M. Tam, B. Novak, and M. Jarrell, *Phys. Rev. E* **98**, 053305 (2018).
- [43] J. Carrasquilla and R. G. Melko, *Nat. Phys.* **13**, 431 (2017).
- [44] S. J. Wetzel and M. Scherzer, *Phys. Rev. B* **96**, 184410 (2017).
- [45] N. Walker and K.-M. Tam, *Mach. Learn.: Sci. Technol.* **2**, 025001 (2020).
- [46] Y. Zhang, A. Mesaros, K. Fujita, S. D. Edkins, M. H. Hamidian, K. Ch’ng, H. Eisaki, S. Uchida, J. C. S. Davis, E. Khatami, and et al., *Nature* **570**, 484–490 (2019).
- [47] D. Lozano-Gómez, D. Pereira, and M. J. P. Gingras, *Phys. Rev. Res.* **4**, 043118 (2022).
- [48] T. Mano and T. Ohtsuki, *JPSJ* **86**, 113704 (2017).
- [49] M. J. S. Beach, A. Golubeva, and R. G. Melko, *Phys. Rev. B* **97**, 045207 (2018).
- [50] E. Khatami, E. Guardado-Sanchez, B. M. Spar, J. F. Carrasquilla, W. S. Bakr, and R. T. Scalettar, *Phys. Rev. A* **102**, 033326 (2020).
- [51] S. Monaco, O. Kiss, A. Mandarino, S. Vallecorsa, and M. Grossi, *Phys. Rev. B* **107**, L081105 (2023).
- [52] D. P. García, J. Cruz-Benito, and F. J. García-Peñalvo, (2022), arXiv:2201.04093 [quant-ph].
- [53] N. Wrobel, A. Baul, K.-M. Tam, and J. Moreno, *Quantum Rep.* **4**, 574 (2022).

- [54] F. Chollet *et al.*, “Keras,” (2015).
- [55] M. Abadi, A. Agarwal, P. Barham, E. Brevdo, Z. Chen, C. Citro, G. S. Corrado, A. Davis, J. Dean, M. Devin, S. Ghemawat, I. Goodfellow, A. Harp, G. Irving, M. Isard, Y. Jia, R. Jozefowicz, L. Kaiser, M. Kudlur, J. Levenberg, D. Mané, R. Monga, S. Moore, D. Murray, C. Olah, M. Schuster, J. Shlens, B. Steiner, I. Sutskever, K. Talwar, P. Tucker, V. Vanhoucke, V. Vasudevan, F. Viégas, O. Vinyals, P. Warden, M. Wattenberg, M. Wicke, Y. Yu, and X. Zheng, “TensorFlow: Large-scale machine learning on heterogeneous systems,” (2015), software available from tensorflow.org.
- [56] S. Lloyd, M. Mohseni, and P. Rebentrost, arXiv:1307.0411 (2013).
- [57] D. Pastorello, “Quantum classification,” in *Concise Guide to Quantum Machine Learning* (Springer Nature, Singapore, 2023) pp. 69–87.
- [58] H.-Y. Huang, M. Broughton, M. Mohseni, R. Babbush, S. Boixo, H. Neven, and J. R. McClean, *Nat. Commun.* **12** (2021), 10.1038/s41467-021-22539-9.
- [59] W. Cappelletti, R. Erbanni, and J. Keller, *2020 IEEE International Conference on Quantum Computing and Engineering, QCE*, , 22 (2020).
- [60] V. Belis, S. González-Castillo, C. Reissel, S. Vallecorsa, E. F. Combarro, G. Dissertori, and F. Reiter, in *EPJ Web of Conferences*, Vol. 251 (EDP Sciences, 2021) p. 03070.
- [61] P. Sen, A. S. Bhatia, K. S. Bhangu, and A. Elbeltagi, *Plos one* **17**, e0262346 (2022).
- [62] D. K. Park, C. Blank, and F. Petruccione, in *2021 International Joint Conference on Neural Networks ,IJCNN* (IEEE,Shenzhen, China, 2021) pp. 1–7.
- [63] C. Blank, D. K. Park, J.-K. K. Rhee, and F. Petruccione, *Npj Quantum Inf.* **6**, 41 (2020).
- [64] M. Schuld, A. Bocharov, K. M. Svore, and N. Wiebe, *Phys. Rev. A* **101** (2020), 10.1103/physreva.101.032308.
- [65] H. Miyahara and V. Roychowdhury, *Sci. Rep.* **12**, 19520 (2022).
- [66] A. Blance and M. Spannowsky, *JHEP* **2021** (2021), 10.1007/jhep02(2021)212.
- [67] E. Grant, M. Benedetti, S. Cao, A. Hallam, J. Lockhart, V. Stojevic, A. G. Green, and S. Severini, *Npj Quantum Inf.* **4** (2018), 10.1038/s41534-018-0116-9.
- [68] R. LaRose and B. Coyle, *Phys. Rev. A* **102** (2020), 10.1103/physreva.102.032420.
- [69] Y. Du, M.-H. Hsieh, T. Liu, D. Tao, and N. Liu, *Phys. Rev. Res.* **3** (2021), 10.1103/physrevresearch.3.023153.
- [70] Z. Abohashima, M. Elhosen, E. H. Houssein, and W. M. Mohamed, arXiv:2006.12270 (2020).
- [71] S. Y.-C. Chen, C.-M. Huang, C.-W. Hsing, and Y.-J. Kao, arXiv:2011.14651 (2020).
- [72] E. Farhi and H. Neven, arXiv: Quantum Physics (2018).
- [73] Y. Lecun, L. Bottou, Y. Bengio, and P. Haffner, *Proc. IEEE* **86**, 2278 (1998).
- [74] C. Bény, “Deep learning and the renormalization group,” (2013), arXiv:1301.3124 [quant-ph].
- [75] P. Mehta and D. J. Schwab, “An exact mapping between the variational renormalization group and deep learning,” (2014), arXiv:1410.3831 [stat.ML].
- [76] H. W. Lin, M. Tegmark, and D. Rolnick, *J. Stat. Phys.* **168**, 1223 (2017).
- [77] E. D. M. Koch, R. D. M. Koch, and L. Cheng, *IEEE Access* **8**, 106487 (2020).
- [78] S. S. Funai and D. Giataganas, *Phys. Rev. Res.* **2** (2020), 10.1103/physrevresearch.2.033415.
- [79] S. Iso, S. Shiba, and S. Yokoo, *Phys. Rev. E* **97**, 053304 (2018).
- [80] M. Koch-Janusz and Z. Ringel, *Nat. Phys.* **14**, 578 (2018).
- [81] K. Ch’Ng, J. Carrasquilla, R. G. Melko, and E. Khatami, *Phys. Rev. X* **7**, 031038 (2017).
- [82] G. Carleo, I. Cirac, K. Cranmer, L. Daudet, M. Schuld, N. Tishby, L. Vogt-Maranto, and L. Zdeborová, *Rev. Mod. Phys.* **91**, 045002 (2019).
- [83] I. Cong, S. Choi, and M. D. Lukin, *Nat. Phys* **15**, 1273–1278 (2019).
- [84] A. V. Uvarov, A. S. Kardashin, and J. D. Biamonte, *Phys. Rev. A* **102** (2020), 10.1103/physreva.102.012415.
- [85] F. Schindler, N. Regnault, and T. Neupert, *Phys. Rev. B* **95**, 245134 (2017).
- [86] T. Maier, M. Jarrell, T. Pruschke, and M. H. Hettler, *Rev. Mod. Phys.* **77**, 1027 (2005).
- [87] M. Caffarel and W. Krauth, *Phys. Rev. Lett.* **72**, 1545 (1994).
- [88] M. Capone, L. de’ Medici, and A. Georges, *Phys. Rev. B* **76**, 245116 (2007).
- [89] A. Liebsch and H. Ishida, *J. Phys. Soc. Jpn.* **24**, 053201 (2011).
- [90] R. Bulla, T. A. Costi, and T. Pruschke, *Rev. Mod. Phys.* **80**, 395 (2008).
- [91] R. Peters, T. Pruschke, and F. B. Anders, *Phys. Rev. B* **74**, 245114 (2006).
- [92] M. Ganahl, M. Aichhorn, H. G. Evertz, P. Thunström, K. Held, and F. Verstraete, *Phys. Rev. B* **92**, 155132 (2015).
- [93] F. A. Wolf, J. A. Justiniano, I. P. McCulloch, and U. Schollwöck, *Phys. Rev. B* **91**, 115144 (2015).
- [94] D. Bauernfeind, M. Zingl, R. Triebl, M. Aichhorn, and H. G. Evertz, *Phys. Rev. X* **7**, 031013 (2017).
- [95] A. Weh, Y. Zhang, A. Östlin, H. Terletska, D. Bauernfeind, K.-M. Tam, H. G. Evertz, K. Byczuk, D. Vollhardt, and L. Chioncel, *Phys. Rev. B* **104**, 045127 (2021).
- [96] M. Potthoff, *Phys. Rev. B* **64**, 165114 (2001).
- [97] H. A. Bethe, *Proceedings of the Royal Society of London. Series A-Mathematical and Physical Sciences* **150**, 552 (1935).
- [98] S. B. Bravyi and A. Y. Kitaev, *Ann Phys (N Y)* **298**, 210 (2002).
- [99] G. Vidal and C. M. Dawson, *Phys. Rev. A* **69**, 010301 (2004).
- [100] M. W. Coffey, R. Deiotte, and T. Semi, *Phys. Rev. A* **77**, 066301 (2008).
- [101] N. Klco, E. F. Dumitrescu, A. J. McCaskey, T. D. Morris, R. C. Pooser, M. Sanz, E. Solano, P. Lougovski, and M. J. Savage, *Phys. Rev. A* **98**, 032331 (2018).
- [102] J. Tilly, H. Chen, S. Cao, D. Picozzi, K. Setia, Y. Li, E. Grant, L. Wossnig, I. Rungger, G. H. Booth, and J. Tennyson,

- Phys. Rep. **986**, 1 (2022).
- [103] R. Dornier, S. R. Clark, L. Heaney, R. Fazio, J. Goold, and V. Vedral, Phys. Rev. Lett. **110**, 230601 (2013).
 - [104] S.-J. Gu, S.-S. Deng, Y.-Q. Li, and H.-Q. Lin, Phys. Rev. Lett. **93**, 086402 (2004).
 - [105] S.-S. Deng, S.-J. Gu, and H.-Q. Lin, Phys. Rev. B **74**, 045103 (2006).
 - [106] J. Spalding, S.-W. Tsai, and D. K. Campbell, Phys. Rev. B **99**, 195445 (2019).
 - [107] J. Carrasquilla and R. G. Melko, Nat. Phys. **13**, 431 (2017).
 - [108] M. Schuld and F. Petruccione, “Quantum models as kernel methods,” in *Machine Learning with Quantum Computers* (Springer International Publishing, Cham, 2021) pp. 217–245.
 - [109] K. Beer, D. Bondarenko, T. Farrelly, T. J. Osborne, R. Salzmann, D. Scheiermann, and R. Wolf, Nat. Commun. **11**, 808 (2020).
 - [110] R. Lippmann, IJNS **5**, 363 (1994).
 - [111] F. Agostinelli, M. Hoffman, P. Sadowski, and P. Baldi, arXiv preprint arXiv:1412.6830 (2014).
 - [112] J. Carrasquilla and R. G. Melko, Nat. Phys. **13**, 431–434 (2017).
 - [113] S. Endo, I. Kurata, and Y. O. Nakagawa, Phys. Rev. Res. **2**, 033281 (2020).
 - [114] R. Sakurai, W. Mizukami, and H. Shinaoka, Phys. Rev. Res. **4**, 023219 (2022).
 - [115] D.-D. Su, X. Dai, and N.-H. Tong, Mod. Phys. Lett. B **27**, 1350034 (2013).
 - [116] S. Sachdev, Physics world **12**, 33 (1999).
 - [117] T. J. Osborne and M. A. Nielsen, Quantum Inf Process **1**, 45 (2002).
 - [118] A. Osterloh, L. Amico, G. Falci, and R. Fazio, Nature **416**, 608 (2002).
 - [119] K. Haule and G. Kotliar, Nat. Phys. **5**, 796 (2009).
 - [120] N. S. Vidhyadhiraja, A. Macridin, C. Şen, M. Jarrell, and M. Ma, Phys. Rev. Lett. **102**, 206407 (2009).
 - [121] S. Kellar, K.-M. Tam, and J. Moreno, Crystals **13**, 106 (2023).
 - [122] S.-X. Yang, H. Fotso, S.-Q. Su, D. Galanakis, E. Khatami, J.-H. She, J. Moreno, J. Zaanen, and M. Jarrell, Phys. Rev. Lett. **106**, 047004 (2011).
 - [123] “Cirq, a python framework for creating, editing, and invoking noisy intermediate scale quantum (nisq) circuits,” <https://github.com/quantumlib/Cirq>.